Signatures of 1.5 MeV leptons in nuclear reactions

Andras Kovacs[1], **Valery Zatelepin**[2], **Dmitry Baranov** [2]

[1]BroadBit Energy Technologies, Espoo, Finland
[2]INLEAS laboratory, Moscow, Russia

E-mail: andras.kovacs@broadbit.com

Abstract. While experimental physics progressed tremendously since the 1970s, the neutron model has remained essentially unchanged. Motivated by developments in both experiments and theory, which we briefly review in section 1, we propose that the initial neutron decay step is not the emission of an 80 GeV mass boson particle, but the emission of a much lighter lepton particle. On the basis of well-known neutron data, in section 2 we estimate that this new lepton's mass is 1.5 MeV.

Historically, investigations of deuteron photo-dissociation led nuclear scientists to assume that no electron-like particle is associated with neutron decay. We therefore re-examine these experiments in section 3. We demonstrate that deuteron photo-dissociation leads to $2p^+ + e^-$ products at high photon energies. Our calculations show why a deuteron always breaks up into $p + n$ particles at <3 MeV photon energy.

Sections 4 - 7 discuss the properties and interactions of the 1.5 MeV lepton particle. Numerous investigations, including our own experiments, demonstrate the presence of negative elementary charges within atomic nuclei. The emission or absorption of negative nuclear charges involves the emission or absorption of a new lepton particle, which always decays into an electron. Various mass measurement methods converge to the same result: the emitted or absorbed lepton is approximately three times heavier than an ordinary electron. Specifically, we measure its mass to be 1553.5 keV.

Our work demonstrates that, despite being a single particle, the neutron comprises a positive and a negative elementary charge. To make sense of the neutron structure, it is necessary to firstly understand the proton's and the newly discovered 1.5 MeV lepton's internal structures. In section 9, we apply our results to better understand the neutron's properties.

1. Motivation

1.1. A brief history of the proton model

Before the 1970s, most scientists viewed the proton as an elementary particle. Starting from the 1970s, scientists working at high energy particle colliders proposed that protons and neutrons are not elementary particles, but comprise smaller sub-particles. According to their model, a proton and a neutron both comprise three quark sub-particles. The existence of quarks has been suggested initially in the 1960s, based on the theoretical efforts by Gell-Mann to model baryons and mesons [3], which were observed in a great variety during high energy nuclear experiments. While Gell-Mann's original quark theory required the F_2 momentum distribution to peak at $x = \frac{1}{3}$, reference [6] demonstrates that this is not the case because the experimentally observed F_2 peak is at $x = \frac{1}{9}$. This deviation from the required peak at $x = \frac{1}{3}$ was explained away

via the hypothesis that the three quarks originally thought to form the proton are the so-called "valence quarks", which are swimming in the background of "sea quarks" [4]. These so-called sea quarks are a collection of quark-antiquark pairs, radiated by the three valence quarks. However, the calculations of 1970s still showed that the valence quarks together with the sea quarks only accounted for 54% of the proton's momentum [2]. A further hypothesis was added to supplement the momentum shortfall of the quarks; chargeless particles called gluons were introduced into the proton model [5]. Since gluons have no electric charge, the thinking was that they are there, but the electrons probing the proton in deep inelastic scattering cannot see them. These hypothesized gluons were assigned the missing proton momentum, and the resulting proton model became the quark-gluon model that it is today. But even with this model of "valence quarks" swimming in the background of "sea quarks and gluons", there seemed to be an angular momentum deficit with respect to the measured angular momentum of the proton, and therefore the presence of "virtual strange quarks" was also postulated in the 1990s [7].

Although the quark-based model was inspired by the great variety of mesons, the proposed quark masses do not add up the masses of observed mesons. According to quark proponents, this is explained by a negative binding energy between quarks: any particle's valence quark masses are only a small percentage of the total particle mass, with the bulk of the particle mass coming from particles which represent the binding force: i.e. virtual quarks and gluons. Moreover, the valence quark : virtual quark : gluon mass ratio is allowed to vary from particle to particle in order to match the observed masses. Now what is the physical meaning of negative binding energy? By definition, negative binding energy means a meta-stable bound state. This model implies that individual quarks should be easily observable upon the break-up of their meta-stable binding. However, quark proponents also postulated that the meta-stable bonds between quarks can never be dissociated. It appears that the quark-based proton model has become embraced without any direct evidence, and maintaining it requires a forever expanding list of postulates.

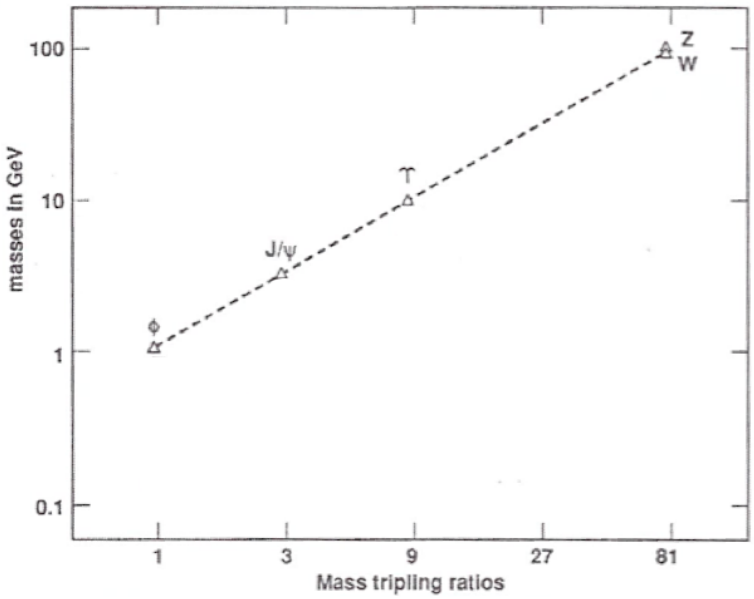

Figure 1.1. The mass tripling pattern of certain mesons, reproduced from [13].

Recently, an electromagnetic proton model has emerged [14], which restores proton's elementary particle status. This proton model employs the same methodology as the successful electron model [9, 25] which gives tangible answers to fundamental questions, such as: what is the electron made of?, what generates the electron's spin?, what is the meaning of the experimentally

measured Compton radius?, and what is the meaning of the experimentally measured classical electron radius? The proton model of reference [14] gives tangible answers to questions, such as: what is the proton made of?, what generates the proton's spin?, what generates the proton's anapole magnetic moment?, and what is the meaning of the experimentally measured proton radius? While the preceding quark-based proton model violates Maxwell's equation via the so-called "renormalization" procedure and proposes complicated interactions among experimentally non-observable virtual particles, which are referred to as "sea quarks" and "gluons", the proton model of reference [14] respects Maxwell's equation and does not require the presence of energy conservation violating virtual particles. The authors of reference [14] demonstrate that their proton model matches all data in high energy electron-proton scattering experiments, without employing postulates or hidden parameters.

The proton's elementary particle status implies that the neutron should comprise positive and negative elementary charges.

Regarding mesons, an alternative modeling approach is to look for simple patterns of their mass variations. As illustrated in figure 1.1, some meson particles form a simple mass-tripling pattern [13]. Coincidentally, our present work demonstrates a similar, but electron related mass-tripling pattern.

1.2. A brief history of the neutron decay model

Regarding neutron decay, it was proposed in the 1970s that the nuclear beta-emission of electrons and antineutrinos is being mediated by 80 GeV mass W boson particles, i.e. an $X_Z^A \rightarrow X_Z^{A+1} + W^-(80GeV) \rightarrow X_Z^{A+1} + e^- + \bar{\nu}_e$ process, which temporarily violates energy conservation. The emission of this 80 GeV mass particle is supposedly allowed by Heisenberg uncertainty; i.e. nucleons are thought activate this uncertainty only above a specific neutron:proton ratio threshold, and keep it de-activated below that threshold. However, it seems to be a violation of the Heisenberg uncertainty principle to model it with an on-off switch.

Presently, claims about the structure and interactions of 80 GeV particles with 10^{-25} sec half-life are highly speculative. Claiming that the emission and absorption of neutrinos is mediated by 80 GeV virtual particles is a particularly extraordinary claim, and should require extraordinary evidence. However, the presence of a W boson was never experimentally observed during neutron decay.

The hypothesis of 80 GeV virtual particles is experimentally contradicted by the beta decay of the ^{163}Dy nucleus. It is known since 1992 that the ^{163}Dy nucleus beta decays in a fully stripped Dy^{66+} state, while the same ^{163}Dy nucleus is stable in a neutral atom [15]. Such beta decay of Dy^{66+} produces a bound state electron, which has a negative energy state with respect to a free electron. While most nuclear theorists insist that any beta decay reaction is completely independent from electromagnetism, it is clear that the electric potential is the controlling parameter of this beta decay process.

If beta decay was triggered by the formation of an 80 GeV mass W boson particle, such process would not care about the presence or absence of orbital electrons. Since the presence or absence of orbital electrons is the actual control parameter of the ^{163}Dy beta decay, it is impossible that any W boson particle is involved in this process.

A similar experimental contradiction is also presented by the beta decay of the ^{210}Bi nucleus. ^{210}Bi beta decays in its ground state, but remains stable in its 271 keV excited state, which is a long-lived excitation state. If beta decay was triggered by the formation of an 80 GeV mass W boson particle, such process would not care about the presence or absence of a nuclear excitation which has 5 orders of magnitude lower energy.

Based on these shortcomings, it is reasonable to consider an alternative model of neutron decays. A more preferable neutron decay model avoids violating any conservation laws.

2. Signatures of 1.5 MeV leptons in neutron decay

Motivated by section 1, we consider what type of particle is released during neutron decays. Since the neutron decay end products are a proton and an electron, this released particle always decays into an electron; i.e. it is some type of a lepton. We refer to this hypothetical lepton as the e_n^- particle.

In a free-particle state, the neutron half-life is 610 seconds. Let us assume that the first step during neutron decay is its transformation into bound p^+ and e_n^- particles. Energy conservation requires the following relationship between these particle masses:

$$m_n = m_p + m_{en} - E_{binding}/c^2 \tag{2.1}$$

$$m_n = m_p + \gamma_L m_{en} - E_{potential}/c^2 \tag{2.2}$$

where m_{en} is the rest mass of released e_n^- particle, and γ_L is the Lorentz boost factor. The above two equations are two equivalent ways of expressing energy conservation.

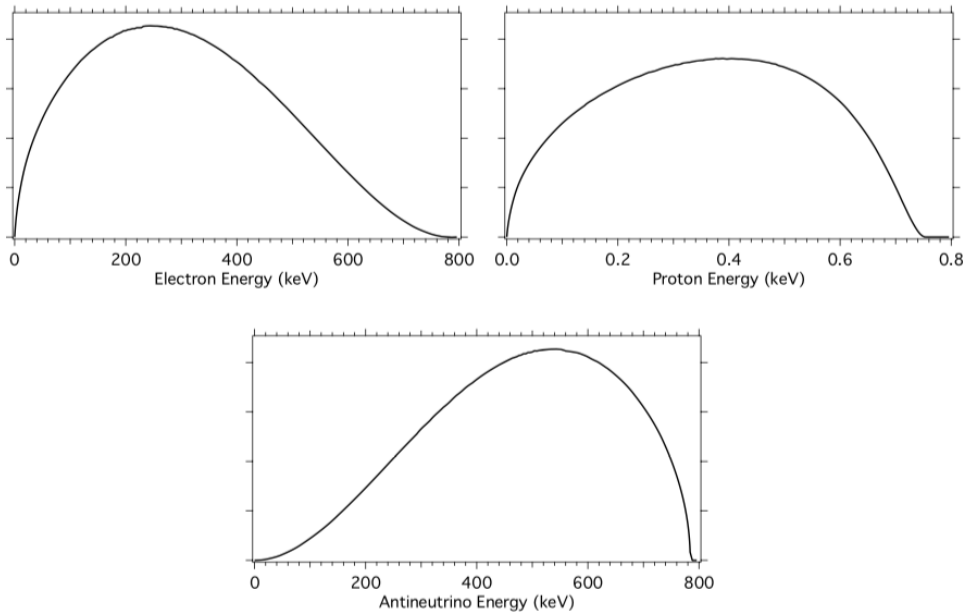

Figure 2.1. Kinetic energy spectra for the electron, proton and antineutrino products of neutron decay (reproduced from [16]).

The bound p^+ and e_n^- particles are in motion relative to each other. At some point, the e_n^- lepton decays into an electron. Momentum conservation must be maintained during the entire decay process.

Figure 2.1 shows the energy spectrum of the final neutron decay products. From the perspective of momentum conservation, is neutron decay a two-body or three-body problem? At one end of the distribution, we have zero antineutrino energy, and thus a two-body problem of momentum conservation. At the other end of the distribution, both the electron and proton have zero momentum; i.e. the neutrino field carries away all the decay energy without impacting any momentum to either the electron or proton. From the perspective of the two charged particles, momentum conservation is therefore a two-body problem at both ends of the distribution spectrum, and we assume that it remains a two-body problem in the entire spectrum.

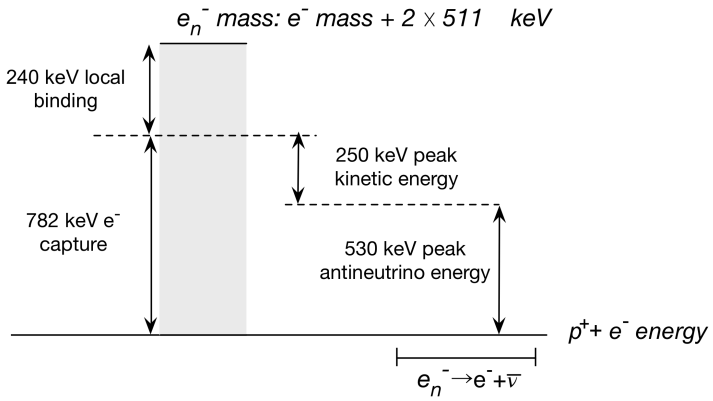

Figure 2.2. The energy diagram of the short-lived bound state between a p^+ and an e_n^- lepton

First estimation of the emitted lepton mass: As the separating p^+ and e_n^- particles must maintain zero net momentum, the ratio between their kinetic energies equals the inverse ratio of their respective masses. We use the peak energy values, which correspond to the highest probability, as the characteristic kinetic energy values. Figure 2.1 shows that the ratio of proton and electron energy peaks is $\frac{250\,keV}{0.4\,keV} = 625 \approx \frac{1836.15}{3} = \frac{m_{p+}}{3m_{e-}}$. This data indicates that the intermediate e_n^- particle is inherently 3 times heavier than an ordinary electron.

Based on the actual neutron mass value, about 240 keV $p^+ - e_n^-$ binding energy would be released if the starting particles are p^+ and e_n^-. Conversely, if the starting particles are an ordinary proton and an electron, the required relativistic electron mass is 240 keV less than 3 electron masses; i.e. the electron must have at least 782 keV energy for neutron formation. Figure 2.2 illustrates the resulting $p^+ - e_n^-$ energy diagram.

3. Signatures of 1.5 MeV leptons in deuteron photo-dissociation

3.1. The historic interpretation of deuteron photo-dissociation

After Chadwick's discovery of the neutron in 1932, there were a lot of discussions whether it is an elementary particle or a hydrogen-like atom formed from electron and proton [1]. For example, Heisenberg and Rutherford were among those who argued that Chadwick's particle is a small hydrogen atom. Pauli however stated that the neutron should be viewed as an elementary particle. To decide who is right, Chadwick's team irradiated deuterons by 2.62 MeV photons, and saw deuterons splitting into a proton and a neutron, without the emission of any electron-like particle. Consequently, most nuclear physicists rejected the nuclear electron concept. With the discovery of the neutron's magnetic moment in 1940, most scientists also rejected Pauli's elementary particle neutron concept, as their elementary particle model assumed the absence of internal charge distribution.

Since deuteron photo-dissociation experiments became a historic water-shed, we now re-examine the methodology and assumptions behind these experiments. The first such experiments were performed by Chadwick and Goldhaber in 1935 [26]: they passed 2.62 MeV gamma rays, emitted by a thorium source, into deuterium gas. The dissociation generated energetic protons with mean proton energy of 0.185 MeV. By conservation of momentum, the other released particle must carry away the same momentum. Since neutrons have about the same mass, a dissociation into a proton and a neutron means 0.185 MeV kinetic energy of the generated neutrons. These values imply a deuteron binding energy of $2.62 - 2 \times 0.185 = 2.25$ MeV. This value matches the experimental deuteron binding energy, measured by photon energy detection upon proton-neutron reactions. Thus the deuteron photo-dissociation into a proton and a neutron has been

proven. Later work showed that the photon energy threshold for deuteron photo-dissociation is 2.26 MeV.

The observation of only proton plus neutron reaction products at this photon energy was historically thought to be a proof for the absence of electron-like particles, based on the idea that energetic photons should primarily ionize away any light particles. The implicit assumption here is that an electron-like particle would more readily interact with >2.26 MeV photons than a proton, and would thus become ionized from the nucleus. We now examine this assumption.

3.2. Deuteron photo-dissociation cross section calculation

3.2.1. The photoelectric effect on nuclear electrons During the chemical photo-dissociation of a H_2 molecule, the radiation field can either break the H_2 molecule into two H atoms [30] or it can ionize the H_2 molecule into an H_2^+ ion and an electron. Analogously, the nuclear photoelectric effect may yield either the ${}^2H^+ \rightarrow p^+ + n$ or the ${}^2H^+ \rightarrow p^+ + p^+ + e_n^-$ reaction pathway. We now determine the relative probability of these two pathways.

Playing with the idea of an emerging electron-like sub-particle, we assume that the radiation field splits the deuteron into bound $p^+ + p^+ + e_n^-$ sub-particles. We start by defining a three-body wavefunction. A reasonable wavefunction model is to consider the three-body wavefunction being a Gaussian function of the sub-particles' distance:

$$\psi = De^{-\frac{\beta}{2}(\mathbf{r}_{p1}-\mathbf{r}_{en})^2}e^{-\frac{\beta}{2}(\mathbf{r}_{p2}-\mathbf{r}_{en})^2}e^{-\frac{\beta}{2}(\mathbf{r}_{p1}-\mathbf{r}_{p2})^2}$$

where $\mathbf{r}_{p1}$ and $\mathbf{r}_{p2}$ denote the two protons' position, and $\mathbf{r}_{en}$ denotes the lepton's position. Such wavefunction maximizes the Shannon entropy of its sub-particles. D and β are two unknown parameters, which can be calculated from two boundary conditions: the deuteron's charge radius is 2.1 fm, and the wavefunction is normalized to a unit probability over the whole space. We thus get $\beta = \frac{1}{24}$ fm^{-2} and $D = 0.0512$ fm^{-3}. The Hamiltonian operator of light-matter interaction is:

$$H = -\sum_i \frac{q_i}{m_i}\hat{\mathbf{A}}\left(\mathbf{r}_i\right)\cdot\hat{\mathbf{p}}_i$$

where q_i, m_i, $\mathbf{r}_i$, and $\hat{\mathbf{p}}_i$ are the given sub-particle's charge, mass, position, and momentum operator, while the $\hat{\mathbf{A}}$ operator corresponds to the electromagnetic wave's vector potential.

Upon photo-dissociation into $2p^+ + e_n^-$ reaction products, the wavefunction of the final state comprises three harmonic functions of the three resulting particles. Using the above Hamiltonian, we calculate the cross-section corresponding to the deuteron wavefunctions' transition from its initial ground state into its final dissociated state. Using 1.5 MeV e_n^- mass, we obtain the orange curve of figure 3.2, which is far below the experimental photo-dissociation cross-section. In the 1930s, theoreticians expected this orange curve to be orders of magnitude higher than the experimental cross-section, mainly because an electron-like particle is much lighter than the other particles. In the light of actually performing the calculation, we can see that it is the low density of states associated with an electron-like particle which causes the ${}^2H^+ \rightarrow p^+ + n$ reaction pathway to have much higher probability than the ${}^2H^+ \rightarrow 2p^+ + e_n^-$ reaction pathway.

3.2.2. The Compton scattering of nuclear electrons At high photon energy, Compton scattering becomes the dominant photo-ionization process of ordinary electrons. Therefore, one cannot neglect the role of Compton scattering in deuteron photo-dissociation. Any particle's Compton scattering cross-section is given by the Klein-Nishina formula. 20-100 MeV photons have much less energy than the proton mass, and thus protons' Compton scattering is negligible in this energy range. On the other hand, this energy range is much higher energy than either the e^- or e_n^- mass. Therefore, according to the Klein-Nishina formula, the e^- and e_n^- Compton scattering

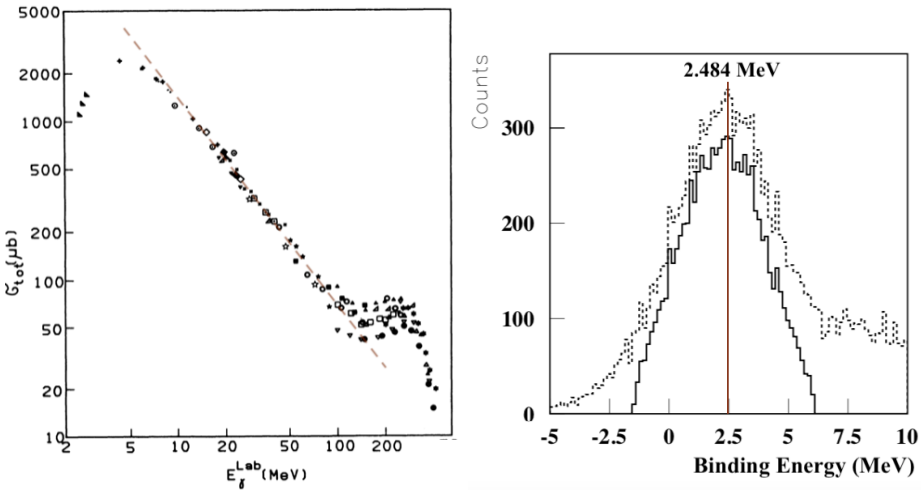

Figure 3.1. Deuteron photo-dissociation by high-energy radiation. Left: the p^+ counting based photo-dissociation cross section (microbarns), as a function of photon energy, reproduced from chapter 6 of [28]. Right: the binding energy among deuteron constituents, measured upon photo-dissociation by 30-50 MeV photons, reproduced from [29].

cross sections vary at the same rate with respect to the photon energy. Within a certain photon energy range, if deuteron photo-dissociation is dominated by the e_n^- lepton's Compton scattering process, then this Compton scattering cross section can be approximated by the total deuteron photo-dissociation cross-section.

The electron's Compton scattering cross-section values at 20 and 100 MeV photon energy are shown in table 1, based on the data of reference [27]. Regarding the e_n^- particle, its Compton scattering cross-section is identified with $\frac{1}{2}$ of the deuteron photo-dissociation cross section in the 20-100 MeV photon energy range. A $\frac{1}{2}$ multiplier must be applied to the p^+ counting based experimental cross-section measurement because the ${}^2H^+ \rightarrow 2p^+ + e_n^-$ Compton scattering produces two protons. The obtained values at 20 and 100 MeV photon energy are displayed in the last column of table 1. As expected, the electron's and nuclear electron's cross sections vary at a similar rate with respect to the photon energy, which is a signature of Compton scattering.

	e^- (Xe)	e^- (Pb)	e_n^- (${}^2H$)
E_γ=20 MeV	14.9 mb	13.7 mb	0.29 mb
E_γ=100 MeV	2.02 mb	1.87 mb	0.035 mb
σ_{20}/σ_{100}	**7.4**	**7.5**	**8.3**

Table 1. A comparison between the e^- and e_n^- Compton scattering cross sections at 20 and 100 MeV photon energy. The millibarn values are the Compton scattering cross-sections of the particles identified in the first row.

When the nuclear electron is removed via Compton scattering, the deuteron breaks up via the ${}^2H^+ \rightarrow 2p^+ + e_n^-$ pathway. Writing this process as ${}^2H^+ \rightarrow p^+ + n \rightarrow 2p^+ + e_n^-$, one may see that such three-body break-up requires 240+2226 keV = 2464 keV energy input. We used here the 240 keV $p^+ - e_n^-$ binding energy estimation obtained in the previous section. As shown in the right side of figure 3.1, the binding energy which was measured upon deuteron photo-dissociation by 30-50 MeV photons indeed peaks at this energy, and not at 2.23 MeV energy. The two curves

peaking at 2.484 MeV only differ in the applied signal filtering condition, which is explained in reference [29].

By comparing the $\boldsymbol{e_n^-}$ and $\boldsymbol{e^-}$ columns of table 1, we can estimate the deuteron-bound e_n^- charge radius according to the following formula:

$$r_{en} = r_e\sqrt{\frac{\sigma_{en}}{\sigma_e}}$$

The data of table 1 yields $2.82\sqrt{\frac{0.035}{1.9}}$ ≈0.39 fm charge radius for the deuteron-bound e_n^-, using the 100 MeV photon energy value. The analogous analysis can be applied also to the ^{3}He isotope: at 100 MeV photon energy its p^+ counting based photo-disintegration cross section is 0.13 mb, and thus its $p^+/3$ counting based photo-disintegration cross section is 0.043 mb. The e_n^- lepton's charge radius calculation according to the above formula yields $2.82\sqrt{\frac{0.043}{1.9}}$ ≈0.42 fm charge radius for the ^{3}He case. The very similar e_n^- charge radii in ^{2}H and ^{3}He further demonstrate that the e_n^- lepton's Compton scattering is the dominating photo-dissociation reaction at 100 MeV photon energy.

Second estimation of the emitted lepton mass: Using 1.5 MeV e_n^- mass and 0.4 fm charge radius parameters, we apply the Klein-Nishina formula, assuming deuteron break-up when the scattered photon deposits >2.484 MeV energy. We thus obtain the red curve of figure 3.2. As anticipated, the Compton scattering cross-section indeed approaches the experimental photo-dissociation cross-section at high photon energies, using $\frac{1}{2}p^+$ counting. In other words, nuclear electrons' Compton scattering dominates deuteron break-up at high photon energies. At 100 MeV photon energy, the $\frac{1}{2}p^+$ counting photo-dissociation cross-section is 0.035 mb, while the e_n^- Compton scattering cross-section evaluates to 0.031 mb. This good convergence validates our 1.5 MeV estimation for the emitted e_n^- mass.

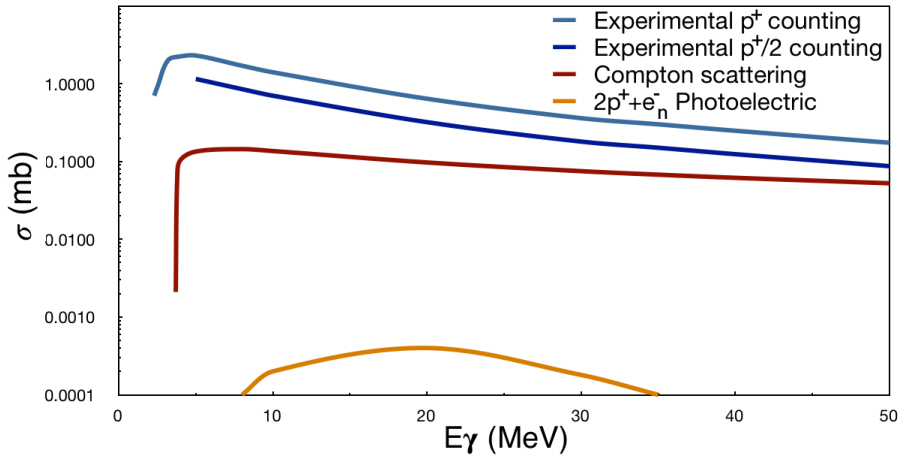

Figure 3.2. The experimental deuteron photo-dissociation cross-section, and the two calculated processes which yield $2p^+ + e_n^-$ dissociation products.

It is important to note from figure 3.2 that the Compton scattering cross section falls to zero near 3.2 MeV photon energy. Below this energy, the only remaining deuteron dissociation reaction is the ${}^2H^+ \rightarrow p^+ + n$ photoelectric process.

3.2.3. Deuteron photo-dissociation summary As seen in figure 3.2, the two processes which yield $2p^+ + e_n^-$ dissociation products rapidly fall to zero in the <5 MeV photon energy range.

Specifically, our calculation shows that the probability of ${}^2H^+ \rightarrow 2p^+ + e_n^-$ reaction is zero when the photon energy is less than 3.2 MeV. Our results clarify why the experimenters of the 1930s saw only $p + n$ photo-dissociation products.

On the other hand, e_n^- Compton scattering becomes the dominant deuteron break-up mechanism when photon energy reaches around 30 MeV. In this photon energy range, the $e^- - e^+$ pair creation process also has a high cross-section. Up to now, experimentalists assumed that any detected electrons originate from pair creation events, thereby not noticing the electrons originating from the deuteron break-up.

4. ${}^4He$ and two e_n^- particles may form a neutral composite

The emission of electrically neutral four-nucleon particles has been observed in various high-energy experiments [11]. The authors of [11] calculate 420 keV binding energy holding such particles together, and they also mention prior experimental studies that obtained the same binding energy value. The scientific literature refers to such four-nucleon objects as "tetra-neutrons", as they were thought to be a meta-stable composite of four neutrons. However, the dissociation of "tetra-neutrons" into individual neutrons has never been observed.

In this section we review experiments which demonstrate that "tetra-neutrons" are in fact short-lived $\left({}^4He + 2e_n^-\right)_{bound}$ particles. In turn, the existence of electrically neutral $\left({}^4He + 2e_n^-\right)_{bound}$ evidences the nuclear presence of this new lepton particle.

4.1. Lead photo-dissociation

The authors of [10] irradiated deuterated materials by 2 MeV photons. They observed deuterium fusion reactions, evidenced by the energetic neutrons that were absent in the hydrated materials based control experiments. The sample materials were enclosed in a lead shielded chamber. These experiments also document the effect of 2 MeV photons on the lead material, but without any interpretation of the obtained results. Here, we focus on the reactions of this irradiated lead material. After some experiment runs, the red signal of figure 4.1 shows the appearance of ^{210}Pb, which is an unstable isotope with 22 year half-life. As can be seen by comparing the red and green signals of figure 4.1, a subsequent irradiation run transmutes ^{210}Pb to ^{214}Pb. This transmutation is evidenced by: i) the disappearance of the ^{210}Pb, ii) the appearance of ^{214}Pb, and iii) the appearance of ^{214}Bi which is a decay product of the short-lived ^{214}Pb.

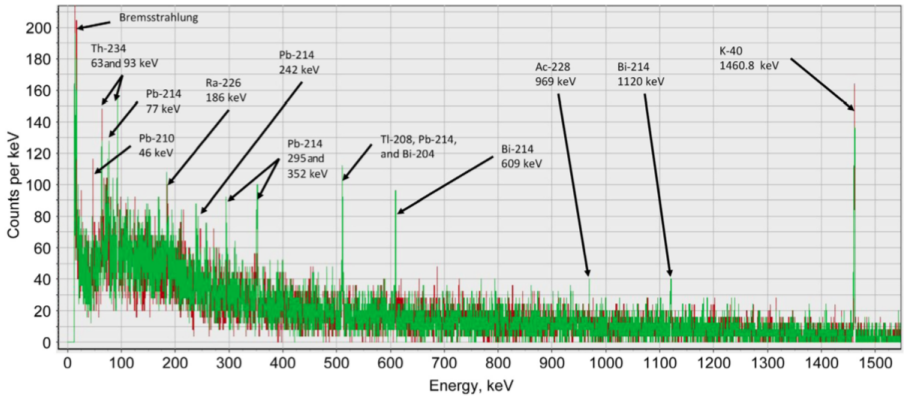

Figure 4.1. The gamma spectrum of an already irradiated lead material, before (red signal) and after (green signal) a 4-hour run of 2 MeV photon irradiation. The signatures of ^{210}Pb to ^{214}Pb transmutation are clearly seen. Reproduced from [10].

How did ^{210}Pb transmute to ^{214}Pb? The involved experiment run was performed with

hydrated sample in the lead chamber, which did not emit neutrons [10]. Regarding the lead material itself, neutron photo-dissociation requires >6.7 MeV for any of its isotopes, which is far larger than the applied photon energy. Moreover, in the case of neutron-induced transmutations we would see the signatures of ^{211}Pb and ^{213}Pb isotopes as well, which have similar half-life and gamma intensity as ^{214}Pb. Therefore, experimental data contradicts individual neutron absorption, and shows that four neutral nucleons were simultaneously absorbed by ^{210}Pb. However, the simultaneous photo-dissociation of four neutrons requires much higher energy than 2 MeV.

What requires less than 2 MeV energy is to strip away an alpha particle and two electrons from any lead isotope. The remaining lead nucleus appears to have lost "four neutrons". In order to generate ^{210}Pb to ^{214}Pb transmutation, the involved alpha particle and two e_n^- particles must be emitted together, as a bound particle:

$$^{208}Pb \quad \overrightarrow{2\,MeV\,\gamma} \quad ^{204}Pb + \left(^4He + 2e_n^-\right)_{bound}$$

The above photo-dissociation scheme is the only reasonable explanation for the observed transmutations, which occur upon the subsequent absorption of $\left(^4He + 2e_n^-\right)$ particles. We note that the resulting ^{214}Pb isotope decays back to ^{210}Pb via the consecutive emission of two electrons and an alpha particle, and never decays via neutron emission.

The appearance of e_n^- leptons during lead photo-dissociation is analogous to their above-discussed appearance during deuteron photo-dissociation.

4.2. The evolution of ^{242}Pu concentration in nuclear reactors

In nuclear reactor cores, ^{239}Pu is produced via a neutron capture by ^{238}U. Further neutron captures generate heavier plutonium isotopes. Starting from ^{238}U, it takes four consecutive neutron captures to get to ^{242}Pu, and thus its concentration should be very low in the initial stages of the fuel cycle. On the other hand, if $\left(^4He + 2e_n^-\right)$ particles were produced in nuclear reactor cores, then ^{242}Pu would be generated via a single capture reaction:

$$^{238}U + \left(^4He + 2e_n^-\right)_{bound} \rightarrow ^{242}U \rightarrow ^{242}Np + e^- \rightarrow ^{242}Pu + 2e^-$$

We discovered in the preceding section that the production of $\left(^4He + 2e_n^-\right)$ particles is triggered by gamma radiation. Gamma radiation is also present in nuclear reactor cores, which motivates examining the concentration of ^{242}Pu in order to determine whether the above reaction takes place. In the absence of the above reaction, the experimental ^{242}Pu concentration must evolve according to the neutron capture calculation. In the presence of the above reaction, the experimental ^{242}Pu concentration must be higher than what is predicted by the neutron capture calculation, especially in the initial stages of the fuel cycle.

A recent study [17] analyzed over 250 fuel samples from multiple reactors, at various stages of burn-up. Under a low burn-up condition of <10 GW-day per fuel ton, the author of [17] finds on average 3 times higher than predicted ^{242}Pu concentration. In the same samples, the average ^{239}Pu concentrations match predictions, which means that the neutron capture calculations are correctly done. The largest concentration excess with respect neutron capture calculations is 400% for ^{242}Pu, while only 39% for ^{239}Pu. These large discrepancies demonstrate that the capture of $\left(^4He + 2e_n^-\right)$ particles is the main source of ^{242}Pu during the initial stages of the fuel cycle.

As the fuel cycles progress, the probability of ^{242}Pu production via four consecutive neutron captures rises steeply. The discrepancy between experimental and predicted ^{242}Pu concentrations becomes gradually smaller with rising burn-up rate [17]. Approximately the same result is found in reference [18]: relative to neutron capture calculations, 15-20% higher experimental ^{242}Pu/^{239}Pu ratio is observed in highly burnt up nuclear fuel. The correctness of the authors'

neutron capture calculation is validated by the matching concentration of other isotopes, such as the ^{146}Nd/^{145}Nd ratio [18]. Consecutive neutron capture thus becomes the main source of ^{242}Pu only in the final stages of the fuel cycle.

In summary, the evolution of ^{242}Pu concentration demonstrates the presence of short-lived $\left({}^4He + 2e_n^-\right)$ particles in nuclear reactor cores.

5. The fission of excited ^{9}Be

The ^{9}Be nucleus comprises two alpha sub-particles, a nuclear electron, and a proton. It takes only 1665 keV to separate a neutron away from it, which is less energy than any of the ^{9}Be excitation energy levels. The energies of its lowest three excited states are shown in figure 5.1. It has been observed that any of these excitations break up the ^{9}Be nucleus with very close to 100% probability [12]. The 1684 keV and 2780 keV excitations decay by neutron emission; the remaining ^{8}Be nucleus then promptly splits into two alpha particles.

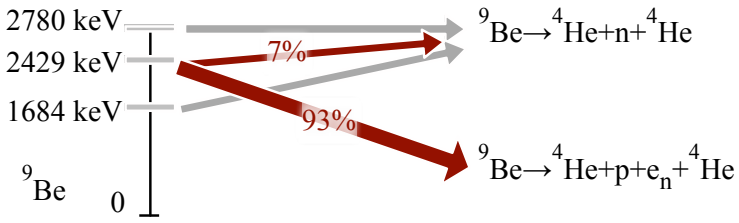

Figure 5.1. The lowest three excitation levels of ^{9}Be and their subsequent break-up reactions.

Interestingly, the 2429 keV excitation decays by neutron emission in only 7% of cases [12]. While, nuclear data tables do not say what break-up products emerge in the other 93% of cases, there is no other possibility than the $^9Be \rightarrow {}^4He + {}^4He + p + e_n$ reaction shown in figure 5.1. The reasons for the impossibility of other reaction products are: i) ^{5}He and ^{5}Li do not exist, and ii) a proton separation into $^8Li + p$ would require over 16 MeV energy. Therefore, the 2429 keV excitation of ^{9}Be decays mainly by emitting a proton and an electron. Such a prompt release of an electron upon nuclear break-up demonstrates that a negative elementary charge must be present in the ^{9}Be nucleus.

6. A precise measurement of the 1.5 MeV lepton mass

In the preceding sections, we found signatures of a 1.5 MeV new lepton which emerges from certain nuclear reactions. Here, we determine its mass more precisely.

It follows from the results of the previous section that negatively charged particles are emitted during the fission of certain excited nuclei. What happens if an emitted e_n^- lepton is captured by another nucleus, prior to its decay into e^-? The nuclear capture of ordinary electrons generates neutrino emission, which is a consequence of the isospin change between the e^- and e_n^- particles. However, if the e_n^- particle's isospin does not change during nuclear capture; its capture may involve just gamma emission. In that case, the binding energy of the e_n^- capture process is emitted as gamma radiation. The measurement of gamma radiation peaks during the nuclear capture of e_n^- is therefore a direct measurement of their binding energy to a given nucleus. On this basis, we seek experimental data of gamma emission from electron capture capable nuclei.

6.1. Nuclear electron capture by ^{58}Ni

The authors of [19] applied hot hydrogen treatment to a nickel metal. They observed unexpected gamma emission from hydrated nickel, and could not explain the source of the obtained gamma

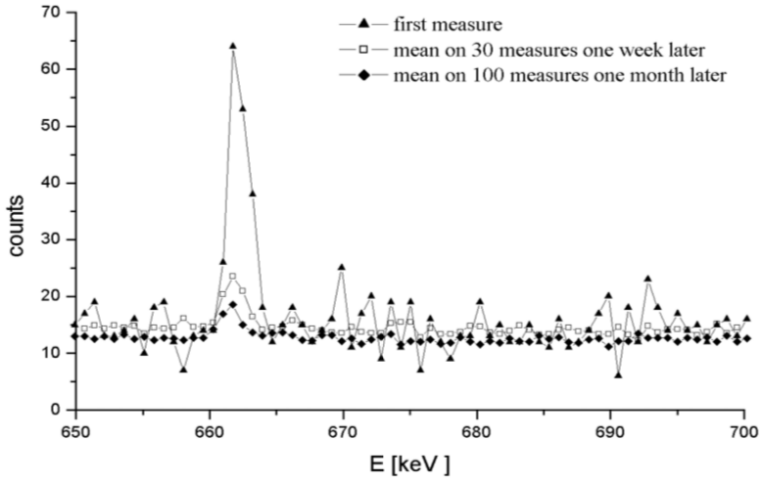

Figure 6.1. The gamma peak corresponding to a nuclear electron capture by ^{58}Ni. Measurement data from [19].

peak. As shown in figure 6.1, this gamma peak is at 661.5 keV. At the same time, they also observed a simultaneous emission of neutrons, at low intensity. Neutron emission is a signature of nuclear fission process. With reference to section 5, a nuclear fission process may involve the release of e_n^- particles as well. We therefore interpret the origin of the gamma peak shown in figure 6.1 as e_n^- capture by certain nuclei.

The ^{58}Ni isotope of nickel is capable of electron capture via the $^{58}Ni + e_n^- \rightarrow {}^{58}Co$ reaction. According to figure 6.1, the binding energy of the e_n^- capture is E_b=661.5 keV. In the case of an ordinary electron, the $^{58}Ni + e^- \rightarrow {}^{58}Co$ reaction is endothermic by E_{ec}=-381.6 keV. Because of the same reaction end product, the difference between E_b and E_{ec} must correspond to the mass difference of the incoming particles. We may therefore determine the e_n^- mass from the following equation:

$$m_{en}c^2 - m_e c^2 = E_b - E_{ec} \tag{6.1}$$

The above equation yields 1554 keV for the e_n^- mass, which matches well the preceding $m_{en} \approx 3m_e$ results.

6.2. Nuclear electron capture by ^1H

We found a second unexpected gamma emission peak during experiments on water vapor under high voltage spark discharges. The measurements were done under air atmosphere, and a shielded chamber was employed to minimize the background noise. The experimental details are given in section 10. This experiment is in fact a laboratory analogue of a natural lightning discharge. The physical processes during lightning discharges have been rather well studied, and several authors noted the production of neutrons by lightnings [20, 21, 22]. The author of [21] discusses similar neutron production by artificial lightning discharges in the laboratory. Via a detailed examination of the lightning process signatures, the authors of [22] determined that the produced neutrons originate from the $^{14}N \rightarrow {}^{13}N + n^0$ fission reaction. The resulting ^{13}N isotope then further decays to ^{13}C. The observation of such fission neutrons yet again signals the possible presence of e_n^- particles as well. We therefore interpret the origin of the gamma peak shown in figure 6.2 as e_n^- capture by some nucleus. This interpretation is further corroborated by a time correlation analysis between the spark discharges and gamma photon emissions, which shows that the peak of figure 6.2 occurs right after each spark discharge, and has microsecond scale duration. The

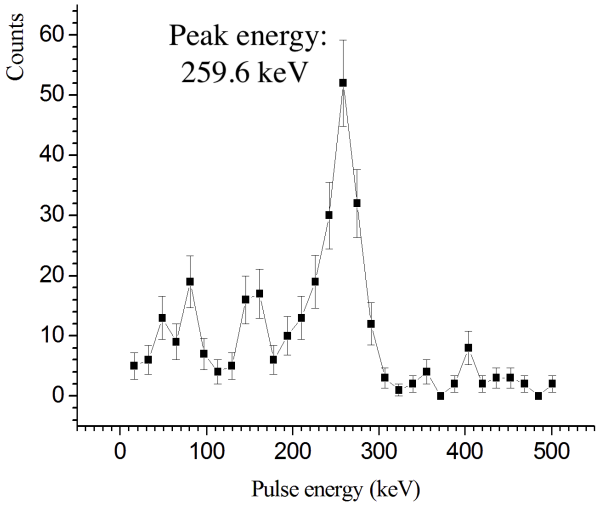

Figure 6.2. The gamma peak corresponding to a nuclear electron capture by a proton. The measurement methods are described in section 10.

details of this time correlation analysis are given in section 10. Therefore the gamma peak cannot originate from any radioactive isotope contamination. Such short duration of the gamma peak emission is characteristic of a free e_n^- particle's short half-life.

Protons are the main electron capture capable nuclei in our experiment, and therefore the capture of nuclear electrons may be written as $p^+ + e_n^- \rightarrow n$. Figure 6.2 shows the measured gamma peak, which implies E_b=259.6 keV binding energy between a proton and a nuclear electron. For ordinary electrons, the $p^+ + e^- \rightarrow n$ reaction is endothermic by E_{ec}=-782.4 keV. We again use equation 6.1 to calculate the nuclear electron mass, and obtain 1553 keV.

Third estimation of the $\mathbf{e_n^-}$ mass: Our precise estimate for the e_n^- mass is the average of the above two measurements, that is $m_{en}c^2$=1553.5 keV.

7. An estimation of the 1.5 MeV lepton half-life in free-particle state

At the JINR institute in Dubna, Vladimir A. Nikitin analyzed pair creation tracks in a bubble chamber, where particle-antiparticle pairs were generated from energetic photons. Upon the analysis of 7000 such tracks, he found nine anomalous lepton tracks. His analysis of these tracks revealed that they are produced by 9±2 MeV particles, that eventually decay into an electron or positron. The 9 MeV lepton is yet another electron-like particle that has been previously unknown. In two cases, the decay event was captured on the track photo. Figure 7.1 shows such a particle pair creation event and the subsequent decay of the negatively charged lepton particle. As can be seen in figure 7.1, the decay process is actually a two-step decay, and an electron is produced upon the second decay step. This electron's track is highlighted by the red circle. The bubble chamber is under 1.5 T magnetic field, and thus we can calculate the electron's momentum from its track radius: its track data yields 1.925 MeV/c momentum. The challenge is to identify the mass of the short-lived intermediate particle.

As can be seen in figure 7.1, the blue circle fitted track of the intermediate particle has three times higher radius than the electron track, and thus its momentum is p_i=5.78 MeV/c.

The track of the 9 MeV lepton is highlighted by the dashed ellipse on figure 7.1. Before its decay, its track is slightly elliptic, which indicates a Larmor precession; i.e. we are observing its

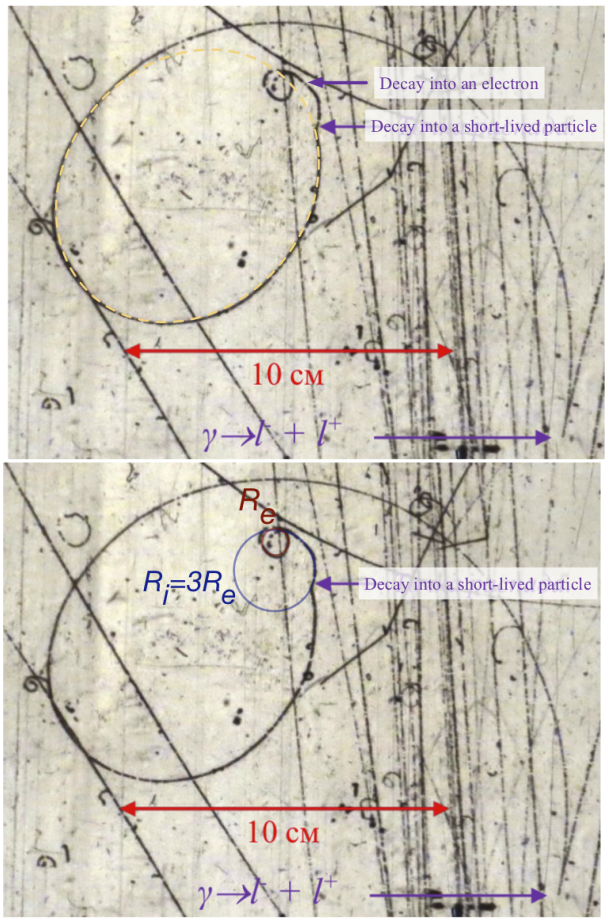

Figure 7.1. Heavy lepton pair creation in a bubble chamber. The 9 MeV lepton-antilepton pair is created at the bottom right corner. The other two purple arrows indicate the two decay events. The yellow dashed ellipse shows the elliptic track fitting of the 9 MeV lepton. The blue and red circles show the circular track fitting of the intermediate particle and final electron, respectively. Photograph provided by V. A. Nikitin.

circular track from a non-perpendicular angle. We use the large elliptic semi-axis to calculate the incoming lepton's momentum, and obtain p_l=21.13 MeV/c. Using the 9 MeV lepton mass value, we obtain a total energy of E_l=23 MeV. During the first decay event, the energy and momentum difference between the incoming heavy lepton and the outgoing intermediate particle are carried away by an anti-neutrino.

Fourth estimation of the e_n^- mass: In this first decay event, the angle between the incoming and outgoing particles is 39°. With respect to the incoming lepton momentum, the outgoing perpendicular momentum is $p_\perp = p_i \sin(39°)$=3.63 MeV/c. The momentum difference in the parallel direction is $p_\parallel$=$p_l - p_i \cos(39°)$=16.64 MeV/c. From the $p_\perp$ and $p_\parallel$ components we calculate the total neutrino momentum: p_ν=17 MeV/c. Since the neutrino mass is negligible, its energy is E_ν=17 MeV. We finally estimate the energy and mass of the intermediate particle:

$$E_i = E_l - E_\nu = 6\ MeV$$

$$m_i c^2 = \sqrt{E_i^2 - (p_i c)^2} = 1.6\ MeV$$

This intermediate particle mass is very close to 1.55 MeV, and therefore we can identify the short lived intermediate particle with the e_n^- lepton. As far as we know, figure 7.1 contains the first photograph of an e_n^- track, although this interpretation must be confirmed by more observations of such events.

Considering the high kinetic energies of the above discussed particles, the intermediate e_n^- speed is close to the speed of light. We can thus make an order of magnitude estimation of its half-life. Considering its track length of about 1.5 cm, it decays after 5×10^{-11} seconds in the laboratory frame. Taking into account the Lorentz boost factor of 4, the e_n^- half-life is in the range of 10^{-11} seconds.

8. A summary of e_n^- properties

Summarizing our results so far, table 2 compares the electron against the newly identified e_n^- lepton.

	e^-	e_n^-
Charge	-1	-1
Mass	511 keV	1553.5 keV
Half-life	stable	$\sim 10^{-11}$ s

Table 2. A comparison between the e^- and e_n^- particles.

The exact ratio between the e_n^- and e^- particle masses is 3.04. In figure 1.1, we illustrated a similar mass tripling pattern among certain mesons. The specific ratio between the J/ψ and ϕ meson masses is 3.038, which is very close to 3.04. Similarly, the ratio between the Υ and J/ψ masses is also very close to this 3.04 value. Perhaps this ratio can be derived from some universal principle, which is valid for both leptons and mesons.

9. Towards a deeper understanding of the neutron

9.1. A single-particle neutron model

The above-discussed experimental data lead to the conclusion that the neutron comprises a positive and a negative elementary charge. How to understand the presence of a negative elementary charge within a proton-like particle? One may wonder whether the neutron is a meta-stable composite of e_n^- and p^+particles. In section 3 we showed that the deuteron's negative charge has 0.4 fm charge radius: this size is comparable to the overall neutron radius, which is around 1 fm. In our view, the neutron's positive and negative charges cannot be considered separate particles from the perspective of spin measurement or momentum uncertainty, because their internal fields mostly overlap. Only in response to very high frequency radiation, which cause Compton scattering, do these charges behave as distinct particles.

For the above reason, we consider the neutron to be a single particle. Within this single neutron particle, the electric field originates from the two well-defined spherical charge surfaces of its positive and negative charges. This electric field is non-zero inside the neutron, and zero beyond the fm-scale range. These intertwined charges generate a shared magnetic field, which is the essential feature of a single-particle neutron model. The neutron's meta-stability means that it eventually splits into bound e_n^- and p^+particles, as discussed in section 2, and then the e_n^- lepton decays into an electron 10^{-11} s later.

One arrives at the single-particle model also from spin entanglement considerations. As derived in the second appendix of [14], three particles with individually measurable spins cannot be in isotropic spin entanglement. In the neutron, the positive and negative charge spins have a fixed relative orientation, which generates the neutron's constant net magnetic moment. A proton's and a neutron's magnetic moments sum up to the deuteron's magnetic

moment, which is also constant. It means that the deuteron's three charges all spin in a fixed relative orientation. Therefore, the deuteron's three elementary charges cannot be particles with individually measurable spins. This indicates that these charges are not distinct particles, i.e. the deuteron's negative charge is not a separate particle from the positive charges. Since the deuteron's negative charge originates from proton-neutron fusion, the neutron's negative charge is not a distinct particle either.

The neutron and deuteron do not have any known excited states. This absence of any excited states is yet another signature of a single particle, despite comprising 2 and 3 elementary charges, respectively.

9.2. The neutron's internal structure

Although we are still in the early stages of understanding the neutron, there is already sufficient experimental data to map out its internal constellation. On the basis of proton experimental data, reference [14] derives the proton's internal structure, which is illustrated on the left side of figure 9.2. Reference [14] derives the following proton parameter set: its major toroidal radius is 0.841 fm, its minor (poloidal) radius is 0.421 fm, and the positive charge's spherical radius is 0.0015 fm.

The neutron's negative charge is imposed over this proton structure. With the advancement of electron-proton scattering measurements, it has become possible to directly map out the neutron's radial charge distribution. Such radial charge distribution data is measured for example at JLAB [24], and is visualized in figure 9.1. The RMS (Root Mean Square) radius value of the positive charge is 0.8 fm, which differs by only 4% from the calculated proton toroidal radius of 0.841 fm. Figure 9.1 conveys the important information that the radial distribution of the neutron's positive and negative charges nearly overlaps; this means that the neutron's negative charge is also at approximately 0.841 fm radial distance from the neutron's center.

The more precise radial distance of the neutron's negative charge can be extracted from so-called "neutron charge radius measurements". Such experiments compare the mean radial distance of the positive and negative charges, and yield $r_n^2 = r_+^2 - r_-^2$=-0.11 fm^2 [31, 32]. Plugging in the above mentioned r_+=0.841 fm value, we obtain r_-=0.904 fm.

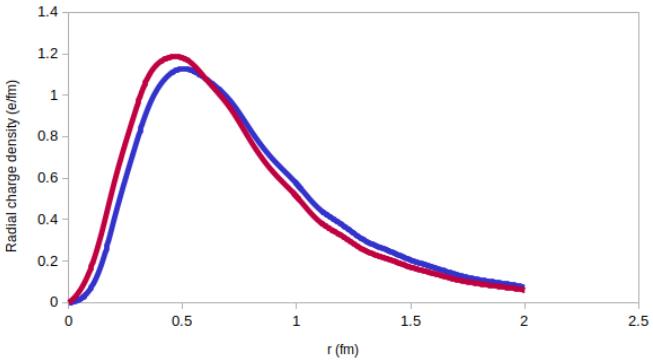

Figure 9.1. The radial density of the neutron's positive (red) and negative (blue) charges, from JLAB measurements [24].

The data of section 3 revealed that the deuteron's negative charge has about 0.4 fm charge radius, and we propose that the neutron's negative charge has the same spherical radius. This proposition is motivated by the observation that a proton's and a neutron's magnetic moments sum up to the deuteron's magnetic moment. This means that during ${}^1H + n \rightarrow {}^2H$ fusion the negative charge merely depolarizes between the two positive charges.

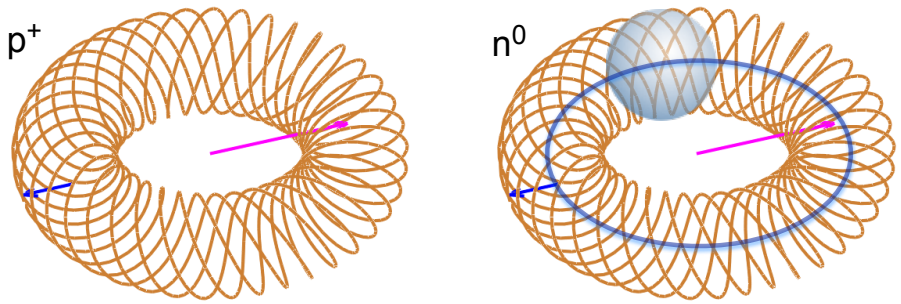

Figure 9.2. An illustration of the toroidal proton structure (left) and the neutron structure (right). The toroidal curve represents the Zitterbewegung path of the neutron's positive charge, and the blue ring represents the Zitterbewegung path of its negative charge. The blue sphere represents its negative charge. Purple arrow: 0.841 fm, blue arrow: 0.421 fm.

Summing up the above information, the neutron's negative charge has approximately 0.4 fm spherical radius, and its center is located at 0.904 fm radial distance from the neutron's center. Fitting the negative charge's spherical radius into the 0.421 fm poloidal radius of the proton structure, we arrive at the neutron geometry illustrated on the right side of figure 9.2[1]. We arrived at this proposed neutron structure by a direct interpretation of experimental data.

We demonstrate the predictive power of this neutron model by calculating the neutron's magnetic moment. The neutron's net magnetic moment comes from two contributions: the $\mu_+ = \mu_p = 2.793\mu_N$ magnetic moment of the toroidal proton structure, and the μ_- contribution of the negative charge. Here, μ_N is the nuclear magneton: its value corresponds to circular Zitterbewegung at $r_N = r_C\frac{m_e}{m_p}$=0.2103 fm radial distance, where r_C is the reduced Compton radius, m_e is the electron mass, and m_p is the proton mass. A point-like negative charge's Zitterbewegung circulation at r_-=0.904 fm radial distance implies a magnetic moment contribution of $\mu_- = -\mu_N\frac{r_-}{r_N} = -4.299\mu_N$. Since the negative charge is not point-like, we also need to take its anomalous magnetic moment factor into account. The derivation of the anomalous magnetic moment factor can be found in chapter 6 of [25], where the $g = \left(1 - \frac{r_{charge}}{2\pi r_{ZBW}}\right)^{-1}$ formula is derived from the basic principles of general relativity. Thus the more accurate μ_- result is:

$$\mu_- = -4.256\mu_N g_- = -4.299\mu_N\left(1 - \frac{0.4}{2\pi \cdot 0.904}\right)^{-1} = -4.625\mu_N$$

Finally, we estimate the neutron's magnetic moment as the sum of the positive and negative charges' contribution:

$$\mu_+ + \mu_- = -1.832\mu_N$$

This estimation matches rather well the neutron's experimentally measured $\mu_n = -1.913\mu_N$ magnetic moment. One may formulate the experimental μ_- value as:

$$\mu_{-,exp} = \mu_n - \mu_p = -4.706\mu_N$$

Our neutron model thus yields a μ_- value that 98% matches the measured one.

[1] As the negative charge's center moves on a ring-shaped Zitterbewegung path, its surface stays within the toroidal volume that is traced out by the positive charge.

9.3. Neutron stabilization by a high electric potential

We saw in section 1.2 that the electrostatic potential is a control parameter of nuclear beta decay. Here, we look into the role of electrostatic potential through the example of ^{17}O. The ^{17}O nucleus is an interesting case for the study of neutron dynamics: it contains a neutron-like sub-particle which is the most similar to a free neutron.

The ^{16}O nucleus comprises four alpha sub-particles. When a neutron is captured by ^{16}O, where will it reside? Considering that the charge radii of ^{16}O and ^{17}O are the exactly same, the captured neutron must be located in the nuclear center, surrounded by four alpha sub-particles. Since the magnetic moment of ^{16}O is zero, the magnetic moment of ^{17}O can be attributed to the captured particles. Interestingly, the magnetic moment of ^{17}O is nearly the same as the neutron's magnetic moment. Specifically, the ^{17}O magnetic moment is $-1.894\mu_N$, which 99% matches the neutron's $-1.913\mu_N$ magnetic moment. These data indicate that the ^{17}O nucleus contains a freely rotating neutron at its center, as schematically illustrated in figure 9.3[2].

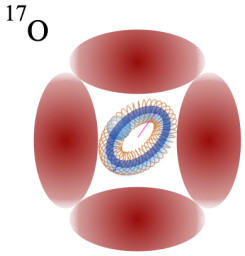

Figure 9.3. The ^{17}O nuclear structure. A neutron is in the center position, the red ellipses illustrate alpha sub-particles.

^{17}O is a stable particle. The neutron at its center cannot decay, because the electron capture energy of ^{17}F is 2.76 MeV; the positive sign of electron capture energy means that the energy needed to remove an electron from the nucleon's location exceeds the 0.87 MeV maximum electron kinetic energy shown in figure 2.1. In other words a neutron becomes stabilized by being at a sufficiently high electrostatic potential, which prevents the electron's departure.

9.4. Neutron destabilization by a strong magnetic field

We now revisit the discussion of ^{9}Be excited states. As noted in section 5, the 2429 keV excitation of ^{9}Be decays mainly by emitting a proton and an electron, in contrast to the neutron-emitting 1684 keV and 2780 keV excitations. Therefore, the break-up of the neutron at 2429 keV excitation is controlled by some other parameter than just the excitation energy.

The ^{9}Be ground state has $J = \frac{3}{2}-$ rotational quantum number designation. Here, the "-" sign denotes the currently popular conjecture of a "negative parity state", which means that the nuclear wavefunction supposedly changes its sign upon the mirror reflection of spatial coordinates. The above-mentioned 2429 keV excited state has $J = \frac{5}{2}-$ rotational quantum number designation. Recognizing this pattern as a rotational series, the next rotational state is $J = \frac{7}{2}-$, and the corresponding excitation energy is 6380 keV. The rotational Hamiltonian's eigenvalues are:

$$E_J = J\,(J+1)\,\frac{\hbar^2}{2I} \tag{9.1}$$

[2] While the ^{4}He charge radius is 1.7 fm, the ^{17}O charge radius is less than twice this size; it is only 2.7 fm. Four alpha subparticles thus do not fit into ^{17}O without deformation, and therefore they are represented by ellipses in figure 9.3.

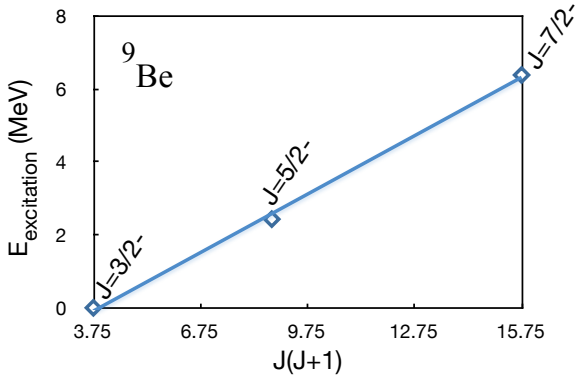

Figure 9.4. The rotational states of ^{9}Be

where E_J is the rotational energy eigenvalue at the rotational quantum number J, and I is the moment of inertia. Figure 9.4 shows the excitation energies as a function of $J(J+1)$. The three data points fit rather well onto a single line, which corresponds to the rotational excitations of a rigid structure. The data shown in figure 9.4 yields $\frac{\hbar^2}{2I}$=534 keV. Considering the 2.5 fm nuclear charge radius of ^{9}Be, this moment of inertia matches quite well the rotation of two alpha sub-particles around each other.

As the positively charged alpha sub-particles rotate around their center of mass, their rotation produces a strong magnetic field. The strength of this magnetic field is proportional to the rotational quantum number J because the moment of inertia remains constant. Since the neutron-like sub-particle breaks up in the $J = \frac{5}{2}-$ and $J = \frac{7}{2}-$ states, a sufficiently strong magnetic field appears to destabilize the neutron. Quantitatively, the magnetic moment values of the various ^{9}Be states are given in table 3. Its first two columns are literature data. Its last two columns are our predictions, calculated from the rotating alpha particles' J states. One may observe from table 3 values that, as a first approximation, the neutron remains stable if the magnetic moment of neighboring nucleons is $<\mu_N$, but becomes unstable if the magnetic moment of neighboring nucleons is $>\mu_N$.

	n	^{9}Be	^{9}Be* (2429 keV)	^{9}Be* (6380 keV)
μ	-1.913μ_N	-1.177μ_N	-0.686μ_N	-0.196μ_N
μ-μ_n	0	+0.736μ_N	+1.227μ_N	+1.717μ_N

Table 3. The magnetic moment of the neutron and various ^{9}Be states, in nuclear magneton units. The last row shows the magnetic moment values without the neutron's contribution.

9.5. The electric binding of neutron decay products

According to the virial theorem, the kinetic energy of a lepton that is electrically bound to a heavier proton is $E_{kinetic} = E_p \frac{\gamma_L}{\gamma_L+1}$, where E_p is the electric potential energy gain and γ_L is the Lorentz boost factor. Using this virial condition together with equation 2.2, we get the following set of equations for the emitted e_n^- lepton:

$$m_n c^2 - m_p c^2 = \gamma_L m_{en} c^2 - E_p$$

$$(\gamma_L - 1)\, m_{en} c^2 = E_p \frac{\gamma_L}{\gamma_L + 1}$$

After expressing E_p in terms of the other parameters, we obtain:

$$m_n c^2 - m_p c^2 = \frac{m_{en} c^2}{\gamma_L}$$

Using the measured $m_{en}c^2$=1553.5 keV value in the above equation, we obtain γ_L=1.2011. Finally, we can calculate the potential and binding energies:

$$E_p = \frac{\gamma_L^2 - 1}{\gamma_L} m_{en} c^2 = 572.5\ keV$$

$$E_{binding} = E_p - (\gamma_L - 1)\, m_{en} c^2 = 260.1\ keV$$

The obtained 99.8% precise match against the binding energy measurement shown in figure 6.2 demonstrates that the neutron decay products are indeed electrically bound during the e_n^- particle's short lifetime. The above calculated potential energy gain implies that the mean $p^+ - e_n^-$ distance is just 2.5 fm.

10. Experimental methods

Figure 10.1 illustrates the experimental setup. The electrode gap with a voltage of 20 kV is placed in a jet of finely dispersed drops of distilled water, supplied from the humidifier by an air stream. This jet of fine droplets is created by high-frequency mechanical vibrations. The pressure in the discharge zone is equal to atmospheric pressure. The discharge gap electrodes are located along the flow of a water-air jet of fine droplets. The flow moves from the cathode to the anode. After passing through the discharge zone, the water-air jet is directed to a ventilation tube, and is released into the atmosphere.

A gamma spectrometer is located above the discharge gap, and consists of a NaI crystal and a Photo-Electrom Multiplier (PhEM). The spectrometer was calibrated by two peaks of the ^{241}Am isotope, which emits gamma rays at 26.3 keV and 59.6 keV energies. These instruments are placed in a lead box with a volume of 15×15×15 cm^3, assembled from 5 cm thick lead blocks.

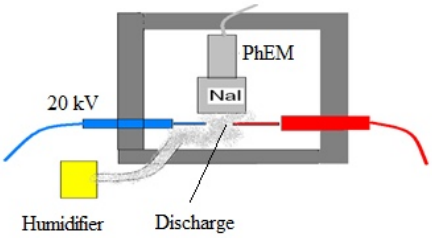

Figure 10.1. The experimental setup for recording gamma radiation during spark discharges in a water-air environment.

By placing the spectrometer and the discharge gap together into a lead box we reduce the gamma background signal in by 40 times, and thus significantly increase the signal-to-noise ratio. Figures 6.2 and 10.2 show the histogram of gamma spectra, which were recorded for 55 seconds. The gamma ray energy is shown along the abscissa axis. Along the ordinate axis, the number of pulses of electromagnetic radiation with a given energy are shown. A peak with an energy of 259.6 keV is clearly visible on figure 10.2. At that 259.6 keV energy, 53 pulses were registered in 55 seconds. When the same spark discharges were done in dry air atmosphere, i.e. without a jet of fine water droplets, no gamma signals were detected above the background.

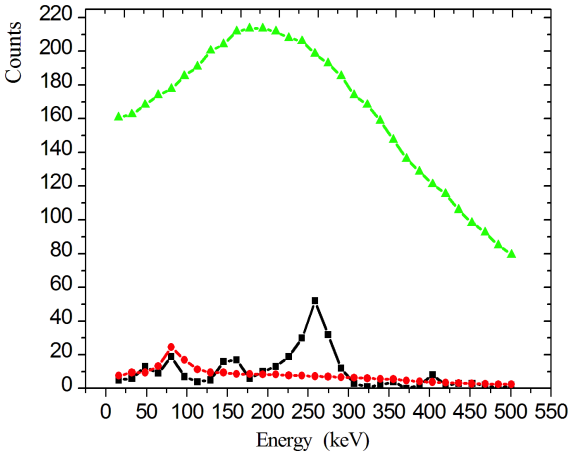

Figure 10.2. A comparison of gamma spectrograms. The black curve was recorded during a 20 kV spark discharge in water-air environment with the recorder located in a lead box, the red curve is the background signal on the recorder located in a lead box while the discharge is turned off, the green curve is the background signal on the recorder located outside the lead box while the discharge is turned off.

Figure 10.2 shows that the background level inside the lead chamber (red curve) is about 10 times lower than the registered peak signal. To the left of the 259 keV peak, another gamma peak with energy ranging from 125 to 175 keV is visible. This side peak provides additional confirmation that the 259 keV peak value is correct, since it is the Compton shoulder of an electron-scattered gamma ray quantum, with the incoming energy of 259 keV.

The green curve of figure 10.2 shows the gamma background in the laboratory area outside the lead chamber. The background outside the lead chamber is about 190 pulses per 55 seconds at 259 keV energy, which exceeds by 3.4 times the peak of the black curve. Therefore, the use of lead box enclosure is essential.

We now address the statistical analysis of the distribution shown in figure 6.2. A direct statistical analysis of figure 6.2 data is complicated by the fact that the NaI crystal has poor spectral resolution. To the left of the 259 keV peak is the Compton shoulder, which distorts the normal distribution of the main peak. Figure 10.3 shows the right branch of the 259 keV peak, which is located far from the Compton peak. This allows us to reasonably apply the normal distribution statistics to the ensemble of experimental points. The red curve shows a normal distribution fitted to the experimental points[3]. It can be seen that the experimental distribution is well approximated by a normal curve centered at 259.6 keV, with a mean squared deviation of 34.7 keV^2. We note that the standard deviation in our experiment is larger than the ± 1 keV deviation shown in figure 6.1, which was recorded by a higher precision gamma spectrometer. Insofar as the gamma peaks of figures 6.1 and 6.2 are signatures of analogous e_n^- capture phenomenon, we can take the higher precision of ± 1 keV as the error margin of table 2 data.

We also investigate the time correlation between the gamma ray signals and the electric discharge sparks. To do this, we use an oscilloscope to register gamma ray signals. In addition, a small radio antenna was also used, located at a distance of 0.5 m from the lead chamber. The oscillograms coming from the two channels of the oscilloscope are jointly analyzed: i.e. the signal

[3] this normal distribution was obtained using the Origin6 software

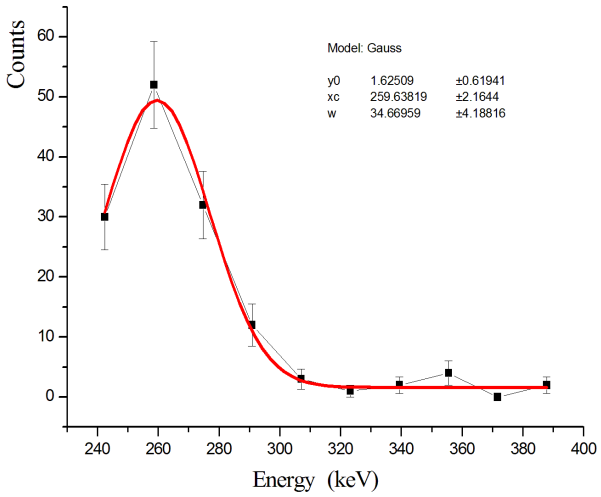

Figure 10.3. The normal distribution curve along the right branch of the 259.6 keV peak. $y0$ is the zero level of the Gaussian along the ordinate axis, xc is the location of the center point, and w is the mean square deviation.

from the PhEM and the signal from the radio antenna. The result of this experiment is a set of oscillograms obtained on the oscilloscope by repeatedly registering short pulses from the NaI detector and from the radio antenna (fast frame mode). The oscillogram recording was triggered when two conditions were met by the gamma signal: i) the duration of the signal is more than 1.5 microseconds, and ii) the signal amplitude is more than 50 mV[4]. Such double condition for starting the oscillogram recording confidently ensures that it starts when the gamma ray quantum passes through the NaI crystal.

Spark discharges generate a bunch of high-frequency oscillations, which were recorded by the radio antenna located 0.5 m away. Each oscillogram shows 25 microseconds before and after the trigger condition. Considering that the sparking frequency is about 10 discharges per second, the probability that a gamma ray quantum and an electromagnetic oscillation signal would both randomly show up in one oscillogram is estimated to be 5×10^{-4}. That is, if the discharge and the formation of a gamma ray quantum are not correlated, then it would take several thousand oscillograms in order to see both signals (i.e from the antenna and from the PhEM) registered in the same oscillogram.

An exemplary oscillogram record is shown in figure 10.4. The green curve shows the signal from the radio antenna; it shows the registration of electromagnetic field oscillations at -9.6 microseconds. It is at this moment that an electric discharge occurs between the two electrodes. These oscillations are almost completed after 5 microseconds, i.e. this is the duration of the spark discharge. The blue curve shows the signal of PhEM; it also reacts to the electromagnetic field like the radio antenna, and shows an oscillating signal at the same time. But 6 microseconds after the spark signal a unipolar negative signal appears on the blue curve, typical for a gamma ray quantum. As explained in the previous paragraph, the probability of a random coincidence between these two signal types is extremely small. We found similar correlated signals on 26% of the recorded oscillograms. Keeping in mind that the oscillogram recording is triggered by any >200 keV gamma ray, i.e. not only the peak signal, we obtain a causal relationship between the

[4] this roughly corresponds to a gamma ray quantum of 200 keV

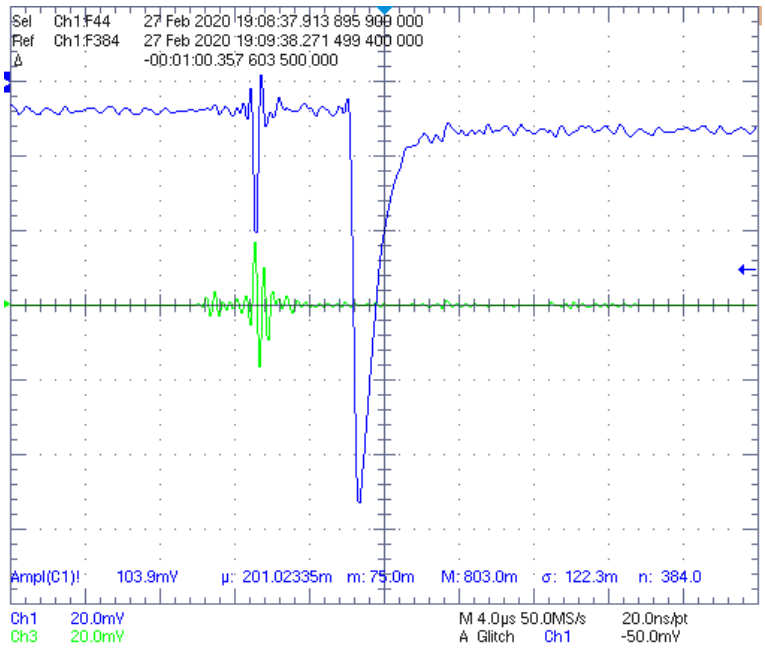

Figure 10.4. An exemplary oscillogram. The blue curve is the PhEM signal, and the green curve is the radio antenna signal. The large negative dip is the signature of a gamma ray quantum.

spark discharges and the 259 keV gamma ray signal.

In summary, the above described analysis proves that the 259 keV gamma peak is statistically significant and it is correlated with spark discharge events in the water-air medium.

We note that this experiment is difficult to replicate because it requires not only thick radiation shielding, but also a large gamma ray sensor and a very short distance between the sensor and the spark discharge location.

11. Conclusions

In conclusion, we presented numerous experimental evidences of a new lepton particle, which is a distinct particle from an ordinary electron. We measured its mass to be 1553.5 keV. It decays into an ordinary electron after just $\sim 10^{-11}$ seconds.

As this 1.5 MeV lepton appears upon neutron decay, it sheds new light on the neutron's internal structure. We proposed a neutron structure that is based on a direct interpretation of experimental data. We conclude that the neutron is a single particle, which is composed of a positive and a negative elementary charge.

Acknowledgements

The work of Andras Kovacs is financially supported by the European Union funded CleanHME project (grant agreement no. 951974). The authors thank Vladimir A. Nikitin for providing the bubble chamber track data.

References

[1] A. Pais "Inward Bound", Clarendon Press (1986), p. 401.

[2] F. Halzen et al "Quarks & Leptons: An introductory course in modern particle physics", John Wiley and Sons (1984)

[3] M. Gell-Mann "A schematic model of baryons and mesons", Physics Letters, Volume 8, 3 (1964)

[4] J. D. Bjorken et al "Inelastic Electron-Proton and γ-Proton Scattering and the Structure of the Nucleon", Physical Review, Volume 185, 5 (1969)

[5] J. Kuti et al "Inelastic Lepton-Nucleon Scattering and Lepton Pair Production in the Relativistic Quark-Parton Model", Physical Review D, Volume 4, 11 (1971)

[6] W. L. Stubbs "The Nucleus of Atoms: One Interpretation", CreateSpace Independent Publishing Platform (2018)

[7] R. L. Jaffe "Where Does the Proton Really Get Its Spin?", Physics Today (1995)

[8] C. van der Leun et al "The deuteron binding energy", Nuclear Physics A, Volume 380.2 (1982)

[9] G. Vassallo et al "The electron and Occam's razor", Journal of Condensed Matter Nuclear Science, Volume 25 (2017)

[10] B. M. Steinetz et al "Experimental Observations of Nuclear Activity in Deuterated Materials Subjected to a Low-Energy Photon Beam", arXiv:1704.00694 (2017)

[11] T. Faestermann et al "Indications for a bound tetraneutron", Physics Letters B, Volume 824 (2022)

[12] Nuclear data tables at www-nds.iaea.org

[13] M. H. MacGregor "The Enigmatic Electron", El Mac Books, 2nd edition (2013)

[14] G. Vassallo et al "The proton and Occam's razor", Proceedings of the 2022 International Association for Relativistic Dynamics (IARD) conference, Journal of Physics - Conference Series (2023)

[15] M. Jung et al "First Observation of Bound-State β^- Decay", Physical Review Letters, Volume 69.15 (1992)

[16] J. S. Nico "Neutron beta decay", Journal of Physics G: Nuclear and Particle Physics, Volume 36.10 (2009)

[17] M. Oettingen "The Application of Radiochemical Measurements of PWR Spent Fuel for the Validation of Burnup Codes", Energies, Volume 15 (2022)

[18] J. S. Kim et al "Analysis of high burnup pressurized water reactor fuel using uranium, plutonium, neodymium, and cesium isotope correlations with burnup", Nuclear Engineering and Technology, Volume 47 (2015)

[19] S. Focardi et al "Evidence of electromagnetic radiation from Ni-H Systems", proceedings of the ICCF-11 International Conference on Condensed Matter Nuclear Science, Marseille, France (2004)

[20] A. V. Gurevich et al "Strong Flux of Low-Energy Neutrons Produced by Thunderstorms", Physical Review Letters, Volume 108 (2012)

[21] L. P. Babich "Thunderstorm neutrons", Physics-Uspekhi, Volume 62.10 (2019)

[22] T. Enoto et al "Photonuclear reactions triggered by lightning discharge", Nature, Volume 551 (2017)

[23] H. Abele "The neutron. Its properties and basic interactions", Progress in Particle and Nuclear Physics, Volume 60 (2008), Pages 1–81

[24] The DOE/NSF Nuclear Science Advisory Committee "The Frontiers of Nuclear Science - A Long Range Plan" (2007)

[25] A. Kovacs et al "Unified Field Theory and Occam's Razor: Simple Solutions to Deep Questions", World Scientific (2022)

[26] J. Chadwick et al "The nuclear photoelectric effect", Proceedings of the Royal Society of London, Volume 151.873 (1935)

[27] E. Storm et al "Photon cross sections from 1 keV to 100 MeV for elements Z=1 to Z=100", Nuclear Data Tables, Volume A7 (1970)

[28] H. Arenhövel et al "Photodisintegration of the deuteron: a review of theory and experiment", Springer (2012)

[29] D. Babusci et al "Deuteron photo-disintegration with polarised photons in the energy range 30–50 MeV", Nuclear Physics A, Volume 633.4 (1998)

[30] Y. Torizuka et al "Entangled pairs of 2p atoms produced in photodissociation of H_2 and D_2", Physical Review A, Volume 99.6 (2019)

[31] H. Atac et al "Measurement of the neutron charge radius and the role of its constituents", Nature communications, Volume 12.1 (2021)

[32] B. Heacock et al "Pendellösung interferometry probes the neutron charge radius, lattice dynamics, and fifth forces", Science, Volume 373.6560 (2021)